Sub-∘C-precision temperature imaging using phase-shift luminescence thermometry

Joel López Bonilla, Frank Beyrau, Benoit Fond

PAPER • **OPEN ACCESS**

Sub-°C-precision temperature imaging using phase-shift luminescence thermometry

OPEN ACCESS
IOP Publishing
Measurement Science and Technology
Meas. Sci. Technol. **36** (2025) 015204 (15pp)
https://doi.org/10.1088/1361-6501/ad846b

Sub-°C-precision temperature imaging using phase-shift luminescence thermometry

Joel López Bonilla[1], **Frank Beyrau**[1] and **Benoit Fond**[1,2,3,*]

[1] Institute of Fluid Dynamics and Thermodynamics, Otto von Guericke University, Magdeburg, Germany
[2] Department of Aerodynamics, Aeroelasticity and Acoustics (DAAA), ONERA The French Aerospace Lab, Paris-Saclay University, Meudon, France
[3] DAAA, ONERA, Institut Polytechnique de Paris, 92190 Meudon, France

E-mail: benoit.fond@onera.fr

Received 24 July 2024, revised 10 September 2024
Accepted for publication 8 October 2024
Published 23 October 2024

Abstract

This work explores the potential of luminescence thermometry to provide temperature imaging with high temperature resolution using the phase-shift method. Phosphor thermometry has been widely used for temperature imaging, especially with the decay-time method. However, the phase-shift method was rarely used. In this approach, excitation is modulated in time, and due to the temperature-dependent luminescence dynamics of the painted luminescent probe, the emission waveform is phase-shifted with respect to the excitation waveform. Initially, a parametric study was performed on the effect of excitation waveform frequency and shape, based on a millisecond-decay time phosphor. The study found that the best precision is achieved with a square waveform at a frequency such that the phase shift is $\frac{\pi}{4}$ at the target temperature. Then, this method was compared with the well-established decay-time method. Phase-shift method offered a three-fold improvement in temperature precision under identical peak excitation power. Finally, two-dimensional measurements were demonstrated on a temperature-controlled plate using a high speed CMOS camera, and an LED illumination. A temperature precision of 0.13 °C was obtained at a temporal resolution of 0.25 s and a spatial resolution of around 1 mm, due to a pre-processing binning of 7 by 7 pixels. This technique can be used as a robust alternative to infrared thermometry to probe the thermal processes with small temperature differences.

Keywords: luminescence thermometry, phase shift, thermographic phosphors

1. Introduction

Temperature measurements are needed to describe thermal systems as they allow to quantify heat transfer rates or to locate heat sources. Specific temperature measurement techniques are available for each application. Thermocouples or resistance temperature detectors are well suited for industrial process monitoring or control. The investigations of complex processes, in particular in model systems, still requires high temporal resolution, multi-point information and minimal perturbation by the probe. For those, optical measurement techniques offer distinct advantages. Infrared thermography is a well-established remote optical thermometry technique. This technique derives temperature from the detected thermal radiation photon flux considering a known surface emissivity. It is capable of high temperature precision at high spatial

* Author to whom any correspondence should be addressed.

resolution [1], with long wave infrared cameras being able to resolve temperature differences smaller than 0.1 °C at ambient temperature [2]. However, it has three principal limitations. First, it can suffer from emissivity changes during thermal processes [3]. Second, it is sensitive to contributions from radiation reflections from other surfaces or gases, e.g. contributions from soot radiation in combustion applications. Finally, windows must be made of infrared transmissible material, e.g. sapphire.

Luminescence thermometry is another type of remote optical thermometry technique. It is based on coating a layer of temperature-sensitive materials (e.g. thermographic phosphors) onto the surface of interest and exploiting the temperature-dependent luminescent properties of such materials upon excitation from a laser or a light-emitting diode (LED) [4, 5]. This technique offers two main advantages over infrared thermography. First, the ability to discriminate spatially, temporally, and spectrally against direct or reflected thermal radiations or emission from gaseous species, e.g. in combustion applications [6]. Second, the fact that many of these materials can be excited and emit in the near UV or visible region. In these regions, liquid water and frost are transparent, enabling measurements on wet or frosted surfaces. Furthermore, standard borosilicate glass is also transparent, allowing the use of inexpensive windows, unlike infrared transmissible windows. Luminescence thermometry can be approached using the intensity method, which directly exploits the intensity changes of the luminescence with temperature due to thermal quenching. This yields a high signal-to-noise ratio (SNR) temperature measurements, making it useful for aerodynamics research, such as detection of boundary-layer transition location on airfoils or wing models, with a temperature precision better than 1 K [7]. However, because the intensity changes are evaluated respect to a reference condition of known uniform temperature, the technique is sensitive to variations in the target condition and temporal variations in illumination and luminescence [4]. Other luminescence thermometry approaches use self-referenced strategies, which are divided into two categories: spectrally-resolved and time-resolved methods [5, 8].

The intensity ratio approach is the most practical and important spectrally-resolved method. It detects two spectral bands of the emission spectrum, which are chosen so that the ratio of the integrated intensities of those bands is temperature dependent. As for time-resolved methods, they can be approached in time or frequency domain. The time domain approach observes the temporal decay of the luminescence intensity after the end of an excitation pulse. This temporal decay is usually approximated with a single exponential behaviour [9] to extract a single scalar, the decay time constant, which is a function of temperature. The decay-time method was found to be less sensitive to optical alignment than the two spectral bands method, since it requires only a single detector [10]. In addition, at temperatures above the onset of thermal quenching of the phosphor, the decay time decreases rapidly with temperature [5], which typically results in higher temperature sensitivity than using spectral changes.

The frequency domain approach also exploits the temperature dependence of the luminescence transition lifetimes, but unlike the decay-time approach, which is typically based on short light pulses separated by many luminescence decay-time constants, it uses a continuously modulated excitation light. Here, the phase shift ($\Delta\phi$) between the phosphor luminescence emission signal and the excitation signal is evaluated. Assuming a mono-exponential decay, the phase shift is directly related to the decay time (τ), via the modulation frequency (f) as

$$\tan(\Delta\phi) = 2\pi f\tau. \tag{1}$$

The specificity of the phase-shift method is that its value depends directly on the modulation waveform. In contrast, the decay time shows only minor dependency on the duration and frequency of the excitation pulse [11–13].

The first application of the phase-shift method was presented by McCormack in 1981, using a BaClF:Sm^{2+} phosphor excited by an halogen lamp, modulated by a 150 Hz square waveform. It achieved a temperature precision of 5 °C ranging from room temperature to 200 °C [14]. Later, Vitta *et al* [15] used this method to characterise the thermal behaviour of operating white high-power LEDs composed by YAG:Ce^{3+} with an accuracy of 5 °C ranging from 100 °C to 200 °C. In both works, point temperature measurements were performed after calibrating the temperature dependence of the decay time, where $\Delta\phi$ was converted to τ from equation (1). Aizawa *et al* proposed to directly calibrate the phase shift-temperature dependence and developed a point-temperature sensor based on phosphor ruby (Cr^{3+}:Al_2O_3) excited by a UV-LED sinusoidally modulated at 100 Hz, with which they achieved a precision of 1.5 °C ranging from 0 °C to 40 °C [16]. The same phosphor and method were implemented in a two-dimensional temperature measurement system by Schreivogel and Pfitzner [17]. This was part of a technique to investigate jet-impingement heat transfer by measuring the temperature distribution at both surfaces of a transparent acrylic plate. The temperature of the surface in contact with the jet was measured using infrared thermography, while the other surface was imaged, through the plate, using phase-shift phosphor thermometry, with a precision of 1.7 °C ranging from room temperature to 65 °C. Apart from surface measurements, this method was also applied for fluid measurements by Ojo *et al* with BAM:Eu^{2+} phosphor particles seeded in the gas phase, in a point-wise thermographic laser Doppler velocimetry configuration [18]. The particles were excited by a UV laser modulated at 1 MHz. They reported a precision of 8.6 °C at 568 °C [18]. Likewise, this method was also applied to pressure measurements using oxygen-sensitive luminescent probes painted on vehicle models placed in wind tunnels in aerodynamic experiments [19–21].

The aim of this study is to identify a strategy which maximises the temperature precision of surface phosphor thermometry for a given temperature range. For 2D phosphor thermometry, the decay-time method has been widely used [22–26], while the phase-shift method was only used in [17]. One of the objectives of this work is to determine which of these two temporal strategies offers the best temperature precision. The comparison should be based on equivalent excitation and detection conditions, and effective temporal resolution. Several studies showed that the precision with the phase-shift method depends on the excitation parameters such as the modulated frequency, which influences the temperature sensitivity [16, 17, 19, 27] and the modulation waveform, which influences the phase-shift precision [18, 28]. This can be exploited. Hence, in this work, a general framework is provided to predict the evolution of the temperature precision for a given phosphor as a function of these parameters.

To proceed with increasing complexity, first, the parametric study and comparison are performed on point measurements, before implementing the methods in an imaging configuration on a temperature-controlled plate to evaluate the temperature precision and accuracy achievable for 2D measurements.

2. Material and methods

2.1. Phosphor particles

Throughout this study, a single phosphor is considered: Cr^{3+} doped yttrium-aluminium garnet phosphor: $Y_3Al_5O_{12}$:Cr^{3+} (YAG:Cr^{3+}). This phosphor was chosen because it has a long decay time at room temperature ($\sim$2 ms), which can be easily resolved with a high-speed camera. Additionally, it has an excitation band at 450 nm, so excitation can be performed using a blue LED. The luminescence emission is a wide band, centred around 690 nm, which can be efficiently detected by standard silicon-based point or array detectors.

2.2. Experimental setup for the parametric evaluation

Figure 1 presents the experimental setup used for phase-shift and decay-time measurements. As shown, a small stack of YAG:Cr^{3+} phosphor powder (ϕ6 mm $\times$ 5 mm) was housed in a temperature-controlled cell made of an electrically heated copper block.

A blue LED (Thorlabs M455L4), with a centre wavelength at 455 nm, was used for excitation of the phosphor. This was mounted with a spherical lens ($f = 50$ mm) to focus the light on the phosphor sample. The luminescence emission was collected by a non-amplified silicon photodiode (Thorlabs DET100A2) equipped with a spherical lens ($f = 35$ mm), and a 665 nm long-pass filter (Thorlabs FGL665M). The function generator of an oscilloscope (Tektronix MDO3034 - 3AFG) was used to modulate the LED with different frequencies and waveforms. The same oscilloscope was used to visualise and record the luminescence emission signal set with an impedance of 50 kΩ (resulting in a bandwidth of 400 kHz).

2.3. Data processing

The phase shift is determined using a Fast Fourier Transform (FFT) algorithm to compute the Discrete Fourier Transform (DFT). This allows to transform discrete signals (excitation and emission) from the time domain to the frequency domain. The result of the DFT is a discrete frequency spectrum represented by complex numbers, whose angle at the modulated frequency (f) is the phase (ϕ) of the signal. If the DFT is performed on both, excitation and emission signals, the phase shift is obtained from the phase difference. FFT was processed using MATLAB Version: 9.12.0 (R2022a) Update 3. The phase of the signals could also be directly measured using a dual-phase lock-in amplifier but this approach is limited to point measurements.

For each condition, the recorded waveform was segmented into data subsets of set durations, which defines the temporal resolution of the measurements. The subsets contain at least one modulation cycles each. To compare different modulation frequencies at fixed temporal resolution, different numbers of cycles per subset were considered. The number of cycles was defined as the temporal resolution multiplied by the modulated frequency.

2.4. Temperature calibration system

The temperature dependence of the phase shift was studied by varying the temperature of the powder in the copper block shown in figure 1(b), which covers the room temperature to 110 °C temperature range. This system is stable for long measurement durations and allows to make a parametric study varying the modulation frequency at each set temperature.

However, to interpret the temperature sensitivity and other characteristics of the phase shift,the temperature dependence of the decay time was evaluated over a wider temperature range (−100 °C to 340 °C). This allows to accurately determine the parameters of a function, which describes well the physics of Cr^{3+} luminescence in YAG (see equation (4) in section 3.1). To cover such a temperature range, the cell was implemented with a fin that was immersed in a liquid nitrogen bath, as shown in figure 1(c). In this case, the cavity that houses the phosphor was connected to a chamber purged with gaseous nitrogen to prevent condensation on the phosphor. The chamber was accessible by an optical window. In both cells, the temperature of the phosphor was measured with a type K thermocouple, which was inserted into the phosphor powder, 3 mm behind the surface, as shown in the detail A of figure 1(b).

For these calibrations, the phosphor luminescence is collected on the surface of the powder stack, as shown in figures 1(b) and (c), but the phosphor temperature is measured by a thermocouple placed 3 mm behind the surface. This can lead to uncertainty in the measurements, therefore it is important to know how uniform are the temperatures within the phosphor stack. To do this, the temperature distribution within the cylindrical phosphor stack was estimated by a 2D steady state heat transfer simulation in cylindrical coordinates. The simulation considers the surface of copper block in contact with the powder at a fixed temperature. The front surface of the powder

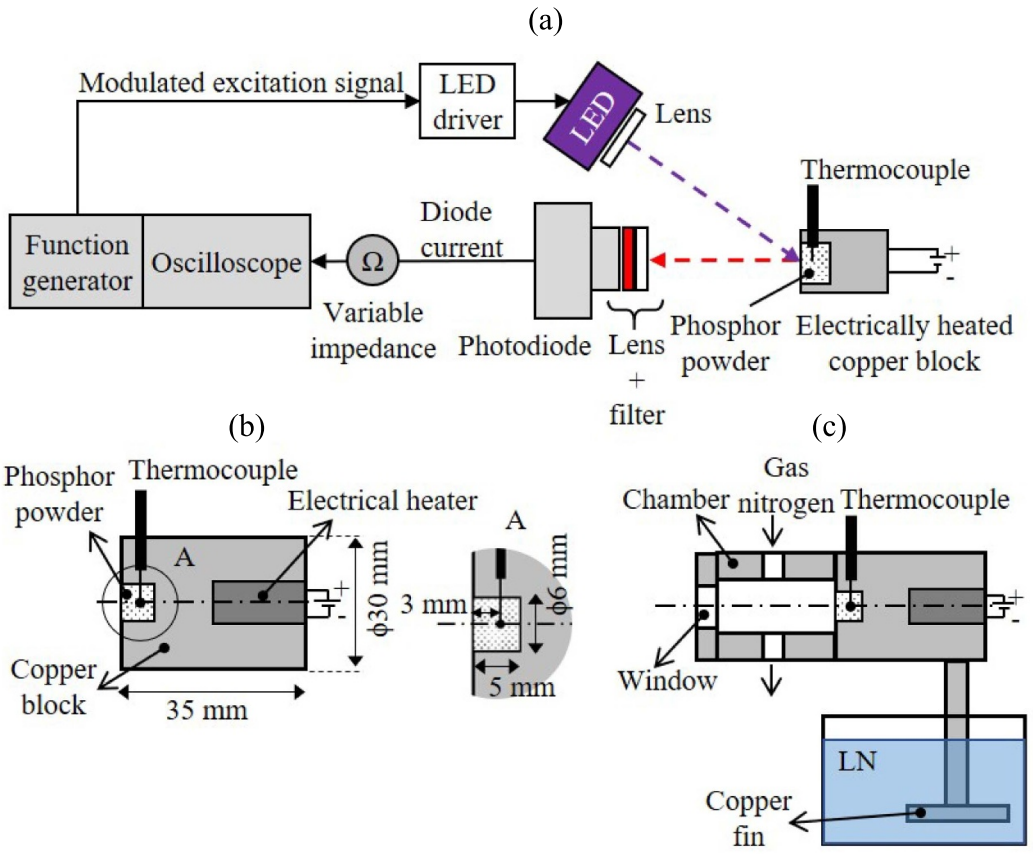

Figure 1. (a) Experimental setup for single-point temperature measurements using phase-shift or decay-time phosphor thermometry. (b) Temperature-controlled cell used for the parametric study (24 °C to 110 °C). (c) Temperature-controlled cell used to calibrate the decay-time response over a wide temperature range (−100 °C to 350 °C).

is considered to exchange heat with the ambient (25 °C) based on Newton's law of cooling. The conductivity of the phosphor powder was assumed to be 0.3 W $(\mathrm{mK})^{-1}$, and the heat transfer coefficient was estimated as 10 W $(\mathrm{m^2K})^{-1}$ (natural convection) for the first system (figure 1(b)), and 7 W $\mathrm{m^{-2}\,K^{-1}}$ (forced convection with a velocity based on the purging nitrogen flow) for the second system (figure 1(c)). The temperature difference between the probed phosphor powder, and the thermocouple was estimated as the difference between the centreline temperature at the front surface and 3 mm within the powder (thermocouple position). The simulations were performed in COMSOL Multiphysics. For the first system, the maximum temperature difference is estimated for a block temperature of 125 °C as 4 °C, or 4% of the ambient-to-block temperature difference. For the second system, the maximum temperature difference is estimated for a block temperature of 300 °C as 10 °C, or 3.3% of the ambient-to-block temperature difference. This temperature difference could be largely minimised using thin phosphor coating, over a conductive metal block instrumented with thermocouples.

The uncertainty in calibration temperature was estimated based on two independent contributions, the above-mentioned temperature difference between thermocouple and probed phosphor powder, and the uncertainty of the thermocouple measurement itself, considered to be 2 °C or 1% of the absolute value. It will be reflected in the error bars of the temperature calibration plots.

2.5. Statistical uncertainty of the measured precision

In this paper, we estimate the precision of the measurements (σ_n). To determine the significance of the improvements of this precision when different configurations are compared, we consider the uncertainty associated with the estimation of this quantity, denoted by $\sigma(\sigma_n)$. We estimate this uncertainty as:

$$\sigma\left(\sigma_n\right) = \frac{1}{2}\sqrt{\frac{2{\sigma_n}^2}{(n-1)}} \tag{2}$$

where n is the number of samples and σ_n is the standard deviation derived from the measurements. The equation is derived from the variance of measured variance ($\mathrm{Var}(\sigma^2) = \frac{2\sigma^4}{(n-1)}$), proposed by [29], for samples that follow a Gaussian distribution. Then, the statistical uncertainty of the measured

precision, considering an interval of confidence of 95%, is plotted as error bars as $\pm 2\sigma(\sigma_n) = \pm\sqrt{\frac{2\sigma_n^2}{n-1}}$.

Note that here only the precision or random uncertainty is considered, as this is the focus of this study. Other sources of uncertainty must also be considered to evaluate the total temperature error, in particular the calibration error, which includes, as discussed in section 2.4, a contribution due to a temperature difference between probed powder and the reference thermometer, and a contribution due to the error in the reference thermometer value.

3. Parametric evaluation of the phase-shift method and comparison to the decay-time method

The temperature precision (σ_T) can be decomposed by differentiation as:

$$\sigma_T(K) = \frac{\delta T}{\delta \Delta\phi}\sigma_{\Delta\phi} = \frac{\sigma_{\Delta\phi}\ (\text{rad})}{S_{a,\Delta\phi}\ (\text{rad K}^{-1})} \tag{3}$$

where, $\sigma_{\Delta\phi}$ is the phase-shift precision, defined as the standard deviation of the phase shift, and $S_{a,\Delta\phi}$ is the absolute temperature sensitivity of the phase shift. Thus, to optimise σ_T, it is needed to analyse both terms, independently. First, the absolute temperature sensitivity will be analysed and then, the phase-shift precision.

3.1. Temperature dependence of the decay time

Before studying the absolute temperature sensitivity of phase shift, the temperature dependence of the decay time was examined. The decay time is an intrinsic property of the phosphor and is directly related to the phase shift, as shown in equation (1). Pulses of 10 ms duration were used, and the decay time was extracted by fitting a mono-exponential decay using a non-linear least square method [9]. The evolution of the decay time of the phosphor with temperature, is presented in figure 2. The decay time decreases continuously from 6 ms to 0.2 ms over the investigated temperature range, i.e. −100 °C to 340 °C. The following equation was used to fit the evolution of the decay time under temperature variation. This equation, reported by [30] and [31], is based on two emitting states (E and T) and the energy transfer between them:

$$\tau_{(T)} = \left(W_E + W_T \times e^{(-\Delta E/k_B T)}\right)^{-1}, \tag{4}$$

where W_E and W_T represent the temperature-independent radiative rate from the E and T energy levels respectively, ΔE is the thermal activation in the excited state and k_B is the Boltzmann constant. The resulting parameters for the fit are presented in table 1. Based on the fit, the relative temperature sensitivity of the decay time was derived, by differentiation, over the temperature range and is also plotted in figure 2. As shown, the sensitivity increases to a maximum of 1.16 % K^{-1} at 0 °C and then decreases slowly towards higher temperatures, but is always above 0.3 % K^{-1} over the entire evaluated range.

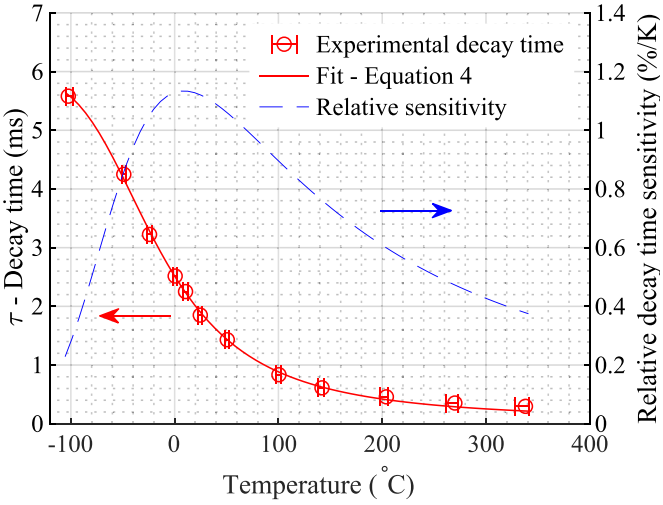

Figure 2. Experimental decay time-temperature characteristics of YAG:Cr^{3+}, fitted with equation (4), and relative sensitivity based on the fitting. Error bars represent the uncertainty of the calibration system that is described in section 2.4.

Table 1. Fitting parameters for the decay time-temperature characteristics based on equation (4).

Parameters	W_E (s^{-1})	W_T (s^{-1})	ΔE (cm^{-1})
	169.8	49 854.8	1012.0

3.2. Temperature dependence of the phase shift

The phase shift-temperature characteristics were measured for different modulation frequencies of sinusoidal waveform. Four modulation frequencies are presented in figure 3. The experimental phase shifts, measured according section 2.3, are fitted with a 3rd order polynomial fit, to guide the eye and to determine the temperature sensitivity. As shown, the phase shift decreases with temperature at any modulated frequency, but the behaviour is different for each frequency. The decay time-based phase shifts, derived from equation (1) and the decay time (presented in figure 2), are plotted alongside the experimental phase shifts. Overall, they show good agreement, especially at low frequencies ($\leqslant$200 Hz). However, discrepancies arises at higher frequencies; at 500 Hz, for instance, the experimental phase shift exceeds the corresponding decay time-based phase shift. An even larger discrepancy was observed at 1000 Hz, but this dataset is not presented because the experimental phase shift was higher than $\pi/2$ (1.57 rad), which is mathematically incompatible with the theoretical equation (1). Such disagreements could be caused by a demodulation at high frequencies. The higher the frequency, the shorter the excitation rise time and, therefore, the lower

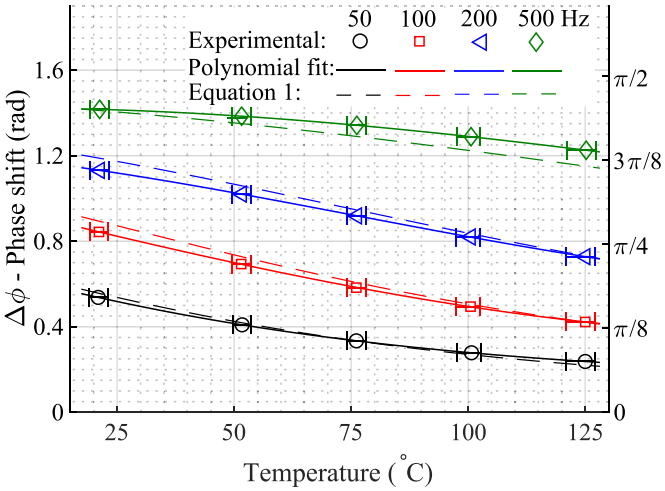

Figure 3. Phase shift-temperature dependence for different modulated frequencies. Experimental data, 3rd order polynomial fits to derive temperature sensitivity and decay time-based phase shift from equation (1) are plotted. Error bars represent the uncertainty of the calibration system that is described in section 2.4.

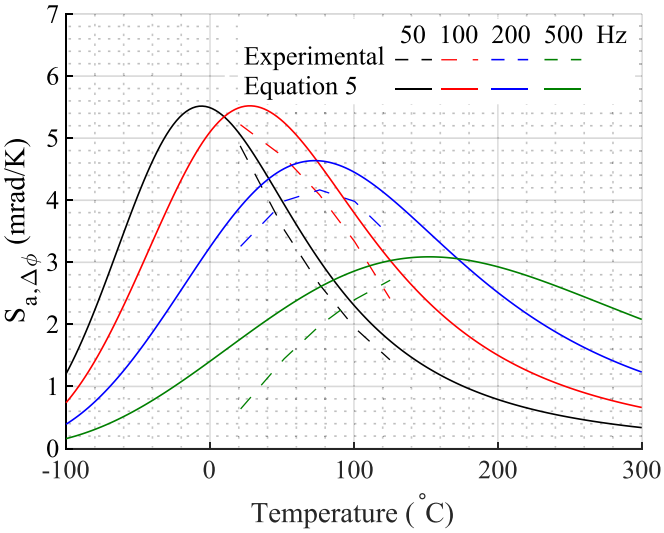

Figure 4. Measured absolute temperature sensitivity of the phase shift for different temperatures and modulated frequencies. Absolute sensitivity derived from equation (5) is also plotted.

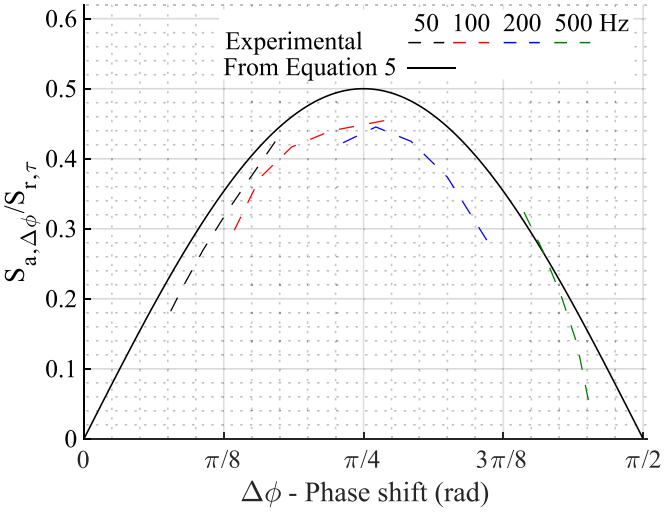

Figure 5. Experimentally-derived sensitivity factor for different modulated frequencies and the sensitivity factor from equation (5).

the amplitude of the phosphor emission. Also, at higher frequencies, the modulation period can be shorter than the correspondent decay time, which leads to incomplete decaying or overlapping of luminescence signal and excitation signal.

3.3. Temperature sensitivity of the phase shift

From these results, the absolute temperature sensitivity of the phase shift ($S_{a,\Delta\phi}$) can be evaluate. This was experimentally determined from the polynomial fits in the phase shift-temperature dependence curves (figure 3) and is presented in figure 4. It is evident that the absolute sensitivity depends not only on the temperature, but also on the modulated frequency, as already reported by [27]. For an interpretation and a generalisation of the trend, we can also consider the sensitivity derived from differentiating equation (1) as in:

$$S_{a,\Delta\phi} = \frac{\delta\Delta\phi}{\delta T} = \left(\frac{\tan(\Delta\phi)}{1+\tan^2(\Delta\phi)}\right)\left(\frac{1}{\tau}\frac{\mathrm{d}\tau}{\mathrm{d}T}\right), \qquad (5)$$

which presents $S_{a,\Delta\phi}$ as a function of the relative decay time-temperature sensitivity, presented in figure 2. This equation, also shown in figure 4, is in good agreement with the measured sensitivity for 50, 100 and 200 Hz, but the deviations are larger at higher frequencies. At any frequency, the sensitivity increases with temperatures to reach a maximum and then it slowly decreases. As the modulation frequency increases, the peak sensitivity decreases and the associated temperature increases. This behaviour can be interpreted by analysing the two terms of equation (5), where the term $\frac{1}{\tau}\frac{\mathrm{d}\tau}{\mathrm{d}T}$ is the relative temperature sensitivity of the decay time and the term $\frac{\tan(\Delta\phi)}{1+\tan^2(\Delta\phi)}$ is the sensitivity factor as it is the ratio of the phase shift's absolute sensitivity and the decay time's relative sensitivity. The relative temperature sensitivity of the decay time ($S_{r,\tau}$), presented in section 3.1, is an intrinsic property of each phosphor, which shows negligible dependence on the excitation waveform (pulse duration [12] or modulation frequency [13]). The sensitivity factor ($S_{a,\Delta\phi}/S_{r,\tau}$) is derived experimentally from the measured absolute phase shift temperature sensitivity (presented in figure 4) and the measured relative decay time sensitivity (presented in figure 2). It is plotted as dashed lines in figure 5 along with the sensitivity factor from equation (5), $\frac{\tan(\Delta\phi)}{1+\tan^2(\Delta\phi)}$. Both are in good agreement and have a maximum at $\pi/4$, showing that equation (5) gives an accurate estimation of the absolute phase-shift sensitivity.

3.4. Phase-shift precision

The second term to evaluate in the temperature precision equation (equation (3)) is the phase-shift precision ($\sigma_{\Delta\phi}$). It

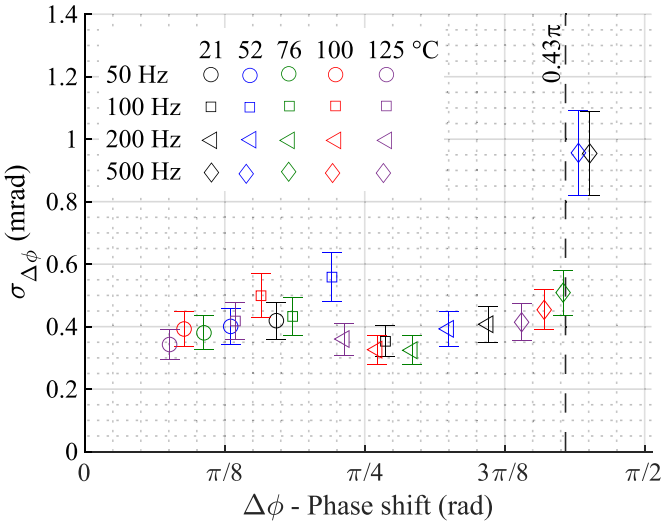

Figure 6. Phase shift precision for different temperatures and modulated frequencies. Error bars are described in section 2.5, based on 100 samples. The temporal resolution is 0.1 s.

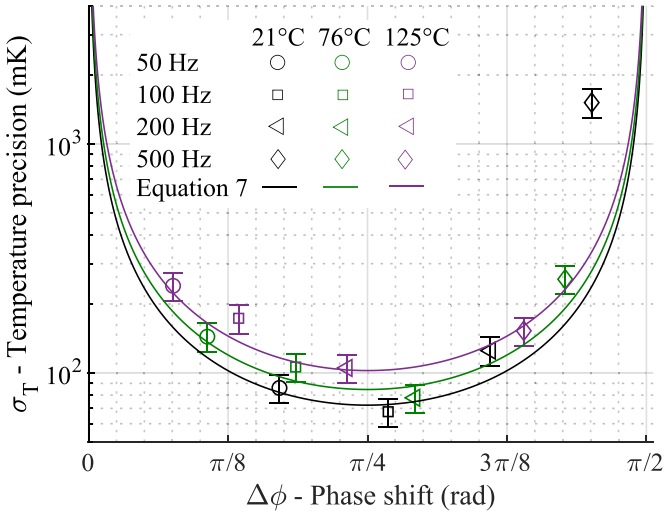

Figure 7. Temperature precision based on equation (7) for three temperature levels as a function of phase shift and the corresponding experimental temperature precision for different modulation frequencies.

generally depends on the experimental conditions. This random phase-shift error is determined as the root mean square (rms) of the phase-shift measurements and is presented in figure 6 as a function of the mean phase shift. It is seen that for a wide range of the phase shift ($\leqslant 0.43\pi$ rad), the precision is nearly constant around 0.4 mrad. At higher frequencies, larger values of the phase-shift standard deviation are measured, as shown in section 3.2. Note that the phase-shift precision here appears to be independent of the temperature. The photophysics of YAG:Cr^{3+} are such that the temperature dependence of the decay time involves two radiative transitions pathways with different rates, with the faster one being activated with increasing temperature [30]. Therefore, the total number of emitted photons is independent of temperature below 300 °C and so the phase-shift precision is also temperature independent.

Therefore, to proceed with the analysis, the phase-shift precision can be assumed constant, which is true for phase shifts $\leqslant 0.43\pi$ rad. This condition can be also expressed as modulation frequency $\leqslant 0.7\tau_T^{-1}$, derived from equation (1). This limits the maximum modulation frequency for a given temperature, where the phase-shift precision can be assumed constant. It is important to mention that the value of the phase shift precision and the region where it can be considered constant are potentially dependent on the level of phosphor emission signal and the sensitivity of the detectors. Then, these parameters need to be determined for different phosphors or detection systems.

3.5. Optimum frequency and prediction of the temperature precision

Thus, $S_{a,\Delta\phi}$ and $\sigma_{\Delta\phi}$ were analysed to continue with the optimization of the temperature precision based on the definition in equation (3). If $\sigma_{\Delta\phi}$ is constant and $S_{a,\Delta\phi}$ is maximized at $\Delta\phi = \pi/4$, then the temperature precision is optimal at $\Delta\phi = \pi/4$. We can then infer, from equation (1), that the optimum frequency ($f_{,\text{Optimum}}$) for a given temperature T is:

$$f_{\text{Optimum}} = \frac{1}{2\pi\,\tau_T}. \tag{6}$$

Furthermore, knowing the value of the phase-shift precision at low phase-shift values, it is thereby possible to predict the evolution of temperature precision, as a function of phase shift and temperature using

$$\sigma_T = G_{\Delta\phi,T} = \frac{(\sigma_{\Delta\phi})_{\Delta\phi_0}}{\left(\frac{\tan(\Delta\phi)}{1+\tan^2(\Delta\phi)}\right)\left(\frac{1}{\tau}\frac{\mathrm{d}\tau}{\mathrm{d}T}\right)_T} \tag{7}$$

where the phase-shift precision, $(\sigma_{\Delta\phi})_{\Delta\phi_0}$, is defined for a given phase shift ($\Delta\phi_0$). In this evaluation, $\sigma_{\Delta\phi}$ is known and constant for $\Delta\phi \leqslant 0.43\pi$. To determine whether equation (7) gives an accurate estimate of temperature precision, it was also experimentally determined as the standard deviation of the temperature datasets obtained by converting the measured phase shift using the 3rd order polynomial fit of figure 3. The results are shown in figure 7 as a function of the phase shift for three different measured temperature levels. The temperature precision determined using equation (7) is also plotted, and shows an excellent fit to the measured data.

Finally, the evolution of the temperature precision over a temperature range for each of the modulation frequencies can be modelled as

$$\sigma_T = G_{f,T} = \frac{(\sigma_{\Delta\phi})_{T_0,f_0}}{\left(\frac{2\pi f\tau_T}{1+(2\pi f\tau_T)^2}\right)\left(\frac{1}{\tau}\frac{\mathrm{d}\tau}{\mathrm{d}T}\right)_T} \tag{8}$$

where the phase shift precision, $(\sigma_{\Delta\phi})_{T_0,f_0}$, is defined for a given temperature (T_0) and modulation frequency (f_0). In this

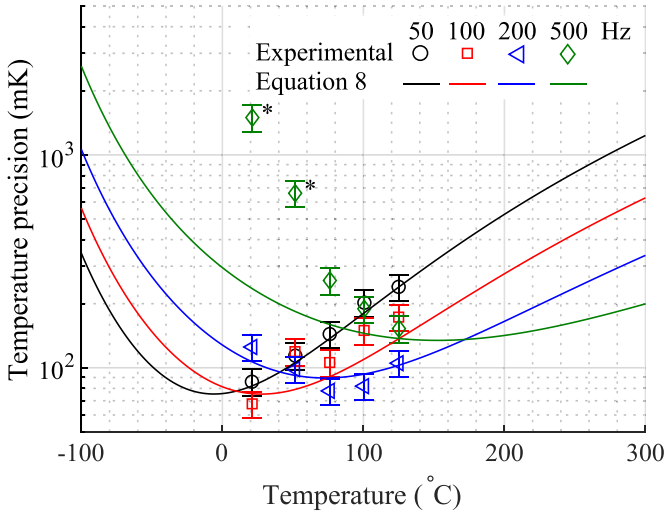

Figure 8. Temperature precision based on equation (8) for different modulation frequencies (f) as a function of temperature and correspondent experimental temperature precision. The datapoints with an asterisk do not fulfil the validity criterion $f \leqslant 0.7\tau_T^{-1}$ for the applicability of equation (8).

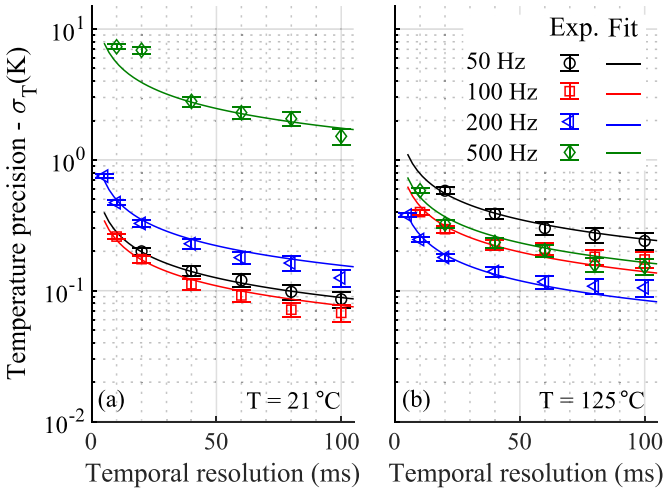

Figure 9. Experimental temperature precision (σ_T) against temporal resolution (δt) for different frequencies at two temperature levels: 21 °C (a) and 125 °C (b). The data was fitted using a relation where σ_T is inversely proportional to $\sqrt{\delta t}$.

evaluation, $\sigma_{\Delta\phi}$ is known and constant for $f \leqslant 0.7\tau_T^{-1}$, as explained in section 3.4.

The precision based on the model in equation (8) and the corresponding experimental data are plotted as a function of temperature in figure 8. The model shows an excellent fit to the measured data. Only the datapoints at 500 Hz and low temperature, marked with an asterisk and whose modulation frequency is lower than $0.7\tau_T^{-1}$ deviate significantly from the model. Therefore, to ensure accurate estimations of the temperature precision, this criterion must be considered.

Figure 8 can be used to design experiments with YAG:Cr^{3+} phosphor. One can find that for a given temperature range, e.g. from 10 °C to 75 °C, the optimal frequency is 100 Hz, which provides a precision better than 80 mK over that range. In this case, the temperature dynamics range of the instrument would be 1:800 for a temporal resolution of 0.1 s.

3.6. Temporal resolution and temperature precision

The temporal resolution, which is defined by the duration of the dataset used to extract a single phase shift, is usually imposed by the application. The temperature precision (σ_T) is plotted in figure 9 as a function of the temporal resolution (δt) for different modulation frequencies and at two different temperatures: 21 °C and 125 °C. The figure shows that for all modulation frequencies, the random temperature error decreases strongly with the temporal resolution. If more cycles are used to extract a single phase, the FFT has more discrete samples to enhance the waveform reconstruction, which improves the measurement. For each modulation frequency, a fit of the form $\sigma_T = K\delta t^{-1/2}$ provides an excellent fit to the data. Therefore, the random error is indeed inversely proportional to the square root of the sample size. Note that the maximum resolution is equivalent to the modulation frequency, since one modulation cycle is necessary to extract the phase shift.

3.7. Square or sine waveform

The shape of the excitation waveform is another parameter that can influence the temperature precision. In this work, the obtained temperature precision using square and sine waveforms are compared at different SNRs: SNR = 10 and SNR = 45. To obtain lower SNR data, the input resistance of the oscilloscope was reduced by factor 5, to 10 $k\Omega$. Measurements were performed at ~25 °C. The evaluated raw luminescence waveforms obtained upon square and sine waveform excitation at 100 Hz modulation frequency are shown in figures 10(b)–(e). Square wave excitation (b and c) leads to a succession of exponential rise and decays, while sine wave excitation (d and e) results in a sine wave emission. The waveforms (c and e) have a higher noise level due to the input impedance reduction. The SNR was calculated as the root mean square of the difference between the measured waveform and a perfectly smooth waveform divided by the waveform amplitude The temperature precision for those waveforms over different levels of temporal resolution is presented in figure 10(a). Clearly, temperature measurements from noisier waveform are less precise than those under higher SNR conditions, regardless of the waveform. At high SNR, the resulting precision is similar for both excitation waveforms. For lower SNR, the temperature precision obtained with square waveform is significantly better than with the sine waveform, with a 35% improvement. This is in agreement with the findings of [18].

3.8. Comparison of decay-time and phase-shift methods

The decay-time method is the most widely used time-domain approach in phosphor thermometry. Therefore, a comparison with the phase-shift method appears to be useful. However, for a fair comparison, both methods should be operated under optimised conditions and at identical temporal resolutions. It is known that the decay-time method performs better with a long

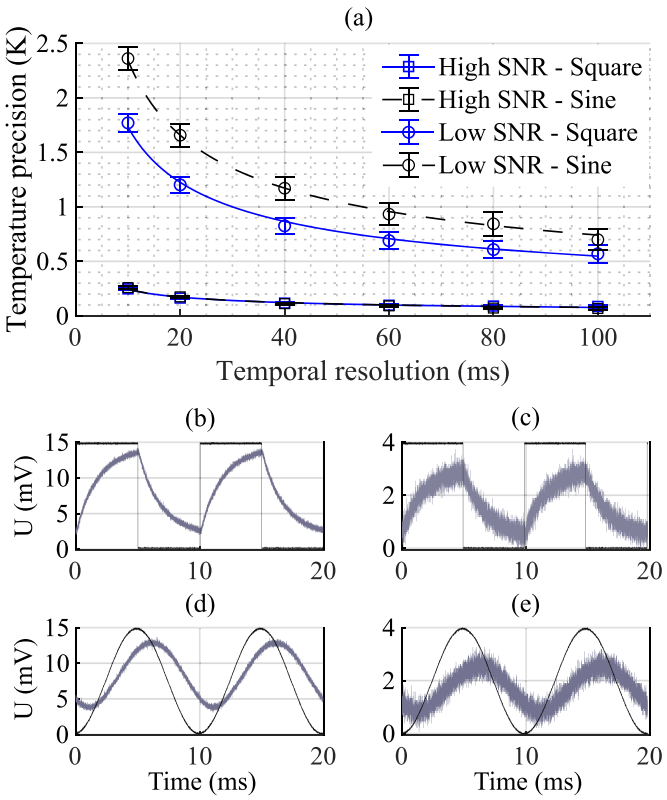

Figure 10. Temperature precision (σ_T) over temporal resolution ($\sqrt{\delta t}$) for square and sine luminescence waveform at two different SNR (a). The data was fitted using a relation where σ_T is inversely proportional to $\sqrt{\delta t}$. Luminescence waveforms (gray) upon square (b) and (c) and sine (d) and (e) excitation waveform (black) at 100 Hz modulation frequency. (b) and (d) show waveforms with SNR = 45, while (c) and (e) show waveforms with SNR = 10.

off-time waveform, as the decay has more time to develop and the evaluation window can be larger.

Three excitation waveforms were considered for a comparison with the sample phosphor powder at room temperature. The first waveform, presented in figure 11(a), is a square waveform (5 ms pulse, 5 ms off-time) at a frequency of 100 Hz with an LED peak current of 0.2 A. This modulation frequency was found, in section 3.3, to maximise the temperature precision at room temperature. The second waveform, in figure 11(c), is a square pulse with a long off-time (1 ms pulse, 9 ms off-time) at the same LED frequency and peak current as for the first waveform. This waveform was used to evaluate the decay-time method. The peak intensity of the luminescence emission is lower in this case because the pulse duration is shorter than in the first waveform. Since the duty cycle of the long off-time tracer is 10%, the LEDs could potentially be driven at a higher current than for the 50% duty cycle square waveform. To represent such a scenario, the third waveform is presented in figure 11(e). This is a long off-time waveform (1 ms pulse, 9 ms off-time) with the LED current raised to 0.5 A. As a result, the peak emission intensity is increased with respect to the second waveform.

The emission waveform was processed for a fixed temporal resolution of 40 ms, corresponding to 4 cycles. The rise and decay time constant were determined using a non-linear algorithm (Levenberg–Marquardt) together with the iteratively-adapted fitting windows algorithm proposed by [9]. The fitting constants, which define the start and end of the windows in each iteration, were optimised to achieve the highest precision.

Figure 11(b) shows that comparing the phase-shift method and decay-time method under the same square waveform results in a 68% improvement in temperature precision when using the phase-shift method. This improvement can partially be attributed to a better photon budget for the phase-shift evaluation, which uses the entire waveform compared to the decay-time method that only uses the decay curve. Therefore, both rise time and decay time were evaluated, and their mean value were considered as a measurement of temperature. The resulting error decreases by 30% with respect to measurements obtained using decay time only. The remaining difference (38%) can be attributed to the fact that the phase-shift method employs a direct linear computation, based on DFT, to determine the phase shift, which has a lower random error than the non-linear algorithm (Levenberg–Marquardt) used to fit the rise or decay curve to a mono-exponential function. Then, for a long off-time waveform at the same LED peak current, in figure 11(d), the precision of the decay time method does not improve due to lower peak intensity owing to the shorter pulse duration. Although non-symmetrical, this waveform can also be evaluated using the phase shift method. However, the precision improvement (15%) is smaller than for the square waveform and falls within the statistical uncertainty of the precision. Finally, when raising the LED current to 0.5 A, in figure 11(f), the precision of the decay time method improves to 183 mK, which is comparable to the 132 mK obtained with the phase-shift evaluation using a square waveform. However, overdriving the LED current is not always feasible.

We also examined the performance of the decay-time method with a fixed fitting window, i.e. non-iterative. For this, a window corresponding to the region where the intensity of the signal is between 10% and 95% the peak intensity was considered. This method was used to extract decay time from the waveforms of figures 11(a), (c) and (e). The results showed a difference in temperature precision of 1%–6% compared to that of the iterative fitting window method. Since this difference falls within the statistical uncertainty of the precision, the results were not shown in figure 11.

The comparison of decay time and phase shift method was evaluated only at room temperature. At this temperature, the modulation frequency of 100 Hz used for the phase-shift method was very near the optimum frequency of 83.7 Hz, where the phase shift is pi/4. To compare the method over a temperature range and not only at that temperature, we modelled the evolution of the precision for both methods with temperature. We assume the phase-shift uncertainty in mrad, and relative uncertainty of decay time in % to be both constant with temperature. This is expected as the total number of

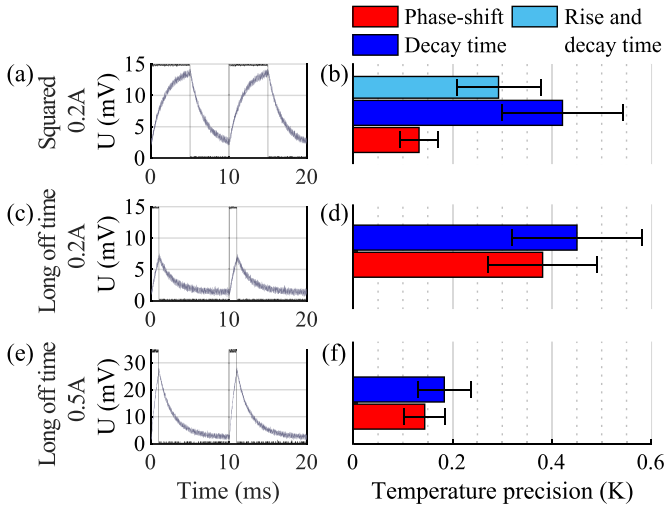

Figure 11. Comparison of the temperature precision using phase-shift and decay-time method for three different excitation waveforms (b), (d), (f). Emission (gray) and excitation (black) signals for symmetrical square excitation (a), long off-time excitation (c) and long-off time excitation with 250% overdriven LED current (e).

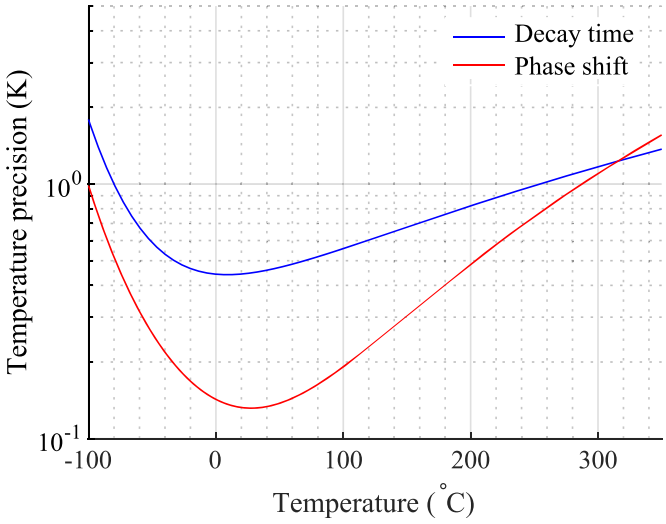

Figure 12. Predicted temperature precision for the phase-shift and decay-time methods over the −100 °C to 350 °C temperature range.

emitted photons per pulse stays, relatively constant, over the −100 °C to 300 °C range, as already mentioned in section 3.4. The precision of the phase-shift method ($\sigma_{T,\Delta\phi}$) is based on equation (8), where $(\sigma_{\Delta\phi})_{T_0,f_0}$ is determined from the precision in (figure 11(b)). The precision of the decay-time method is estimated as $\sigma_{T,\tau} = \frac{(\frac{\sigma_\tau}{\tau})_{T_0}}{S_{r,\tau}}$, where $(\frac{\sigma_\tau}{\tau})_{T_0}$ is determined from the precision in (figure 11(d)) and $S_{r,\tau}$, from equation (4). The results are plotted in figure 12, which shows at the temperature increases, the improvement offered by the phase shift method over the decay time method reduces. This is due to a reduction of the sensitivity factor ($S_{a,\Delta\phi}/S_{r,\tau} = \frac{\tan(\Delta\phi)}{1+\tan^2(\Delta\phi)}$) as the value of $\Delta\phi$ increases, as shown in figure 5. Nevertheless, the decay time performs better over a wide temperature range, from −100 °C to 315 °C.

However, one aspect which must be considered is that the two methods are compared at a fixed temporal resolution corresponding to four excitation waveform cycles. The maximum temporal resolution for the phase-shift method is one excitation cycles (here 10 ms), while the decay time-method can yield results for single pulses. In this case, the temporal resolution would be determined by the fitting window duration, which is generally two decay time constants (here 4 ms). Therefore the decay-time method allows a larger range of temporal resolutions than the phase-shift method. If a higher level of temporal resolution is necessary, a strategy to leverage the enhanced precision of the phase-shift method could be to use a faster decaying phosphor. In Ojo *et al* a phosphor with a decay time in the sub-microsecond range was used together with an excitation waveform frequency of 1 MHz [18].

3.9. Influence of residual scattering light

A potential challenge with the phase-shift method is the fact that luminescence signals during excitation are also exploited, while the decay-time method evaluates only signals when the excitation is off. If contributions from reflected light from the excitation or fast fluorescence from excited compounds or windows remain in the detected signals during the excitation, then this may result in a reduction of the apparent phase shift of the emission signal with respect to the excitation waveform. To evaluate the potential presence of those so-called in-phase signals, the decay time out of the measured phase shift and equation (1) was compared to the decay time measured from the decay curve during the time off. This comparison was performed using the square waveform in figure 11(a). The decay time out of phase shift was calculated as 1.82 ms, and the decay time resolved from the decay curve as 1.77 ms. This makes a difference of 3%, which can represent the presence of a negligible in-phase signal or a potential multi-exponential behaviour. Therefore, using appropriate filters, it is possible to eliminate the contribution of LED reflections, and potential fluorescence signals.

4. Application on a temperature imaging configuration

4.1. Experimental setup

The findings from the parametric evaluation are now applied on a temperature imaging configuration. A schematic of the setup used to perform 2D phase-shift-based luminescence thermometry is presented in figure 13. In this case, the temperature imaging was conducted on a uniform temperature-controlled surface to demonstrate the performance of the approach in this configuration.

For this configuration, the luminescence emission was imaged using a CMOS high-speed monochrome camera (Photron SAX-2) in conjunction with a 50 mm Nikkor f/1.4 lens (Nikon) and a 610 nm long-pass optical filter (Thorlabs FGL610S). The camera was operated at full resolution (1024 × 1024 pixels) at a recording rate of 5 kHz,

and an exposure time of 200 µs. The projected pixel size in the image plane was 0.135 mm corresponding to a field of view of 138.2 mm × 138.2 mm. To avoid room light fluctuations that may interfere with the emission waveform signal, the experiments were conducted in a dark environment. The image acquisition was managed by a programmable timing unit and the software DaVis 8 (LaVision).

The phosphor excitation parameters were set based on the previous evaluation. Considering the decay time (figure 2) for the expected temperature of the surface (30 °C– 40 °C), the optimum modulation frequency was around 100 Hz, according to equation (6) and experimental results from figure 8. Moreover, the square waveform was previously found to exhibit better precision. Therefore, the phosphor was excited by two LEDs (Thorlabs M455L4) modulated at 100 Hz with a square waveform. The LEDs were modulated in phase with the image clock of the camera, using a digital delay generator (Stanford Research Systems DG535). Both LEDs produced an LED output power of approximately 2.8 W with the LED drivers set at maximum current of 1 A.

To achieve a uniform temperature-controlled surface, a steel plate (60 × 100 × 0.5 mm), coated with phosphor, was clamped in a heating unit made of a thick aluminium body with an internal flow of temperature controlled silicon oil through a serpentine-shaped channel, promoting a spatially uniform temperature on the plate. More details about the heating unit can be found in [32, 33]. A thermocouple type K, installed 5 mm behind the plate, measures the oil temperature near the plate. The deviation between the oil temperature and surface temperature of the plate is expected to be less than 0.5 °C based on heat transfer consideration, as reported in [33].

The plate was coated with YAG:Cr^{3+} phosphor using spray coating with a ceramic based binder (HPC from ZYP Coatings, Inc). The layer thickness was estimated to be around 10–20 µm based on micrometre screw gauge measurements of the plate thickness before and after the coating process.

4.2. Image processing

The raw luminescence images were acquired and then background-subtracted using images recorded with the LEDs turned off. Afterwards, an intensity threshold was applied on the images, which results in filtering out pixels with less than 200 counts on the brightest frame of a cycle. Below this level, the modulation was found to degrade. Probable causes for this observation are sensor non-linearity, local paint defects or silicon oil contamination.

Different levels of binning were applied to study the influence of spatial resolution on the temperature precision. To obtain a temperature image, 1250 consecutive images were processed, which represent 25 cycles at 100 Hz or a temporal resolution of 250 ms. The phase of this emission signal on each pixel (or binned pixel) was evaluated using DFT. Regarding the phase of the excitation signal, the LED and start of the camera recording were triggered using the same signal. Therefore, the excitation waveform had a fixed phase in the camera recording time, which was determined by DFT based on an oscilloscope trace.

Additionally, a white (or flat) field correction to the phase-shift field was performed to correct any potential effect of the spatial variations in the paint properties as well as potential effects of the local excitation intensity on the phosphor luminescence dynamics. This white field $\Delta\phi(x,y)_{white}$ is determined as the average of three consecutive independent phase-shift measurements when the steel plate was at room temperature. The white field image was then normalised by division by its spatially averaged value, as in:

$$\varphi(x,y) = \frac{\Delta\phi(x,y)_{\text{white}}}{\Delta\phi_{\text{avg,white}}}. \tag{9}$$

The white field corrections consist of a division by this normalised white phase-shift field ($\varphi(x,y)$), as in:

$$\Delta\phi(x,y)_{\text{corrected}} = \frac{\Delta\phi(x,y)}{\varphi(x,y)}. \tag{10}$$

Finally, the calibration curve (see figure 14) was used to convert the corrected phase-shift field into the temperature field.

4.3. Temperature calibration

A phase shift-temperature dependence, ranging from room temperature (23 °C) to 63 °C, was evaluated by varying the set temperature of the heating unit (figure 13). The temperature calibration curve is presented in figure 14, where the temperature corresponds to the readings of the thermocouple embedded in the temperature controlled unit and the phase shift is the mean value of a small region ($\sim$19 × 19 mm^2) in the centre of the plate. As for the measurements in section 3.2, the phase shift decreases with temperature. The experimental data is fitted with a third order polynomial, with a maximum deviation from the fit of 0.15 °C. The experimental absolute temperature sensitivity, derived from this polynomial fit, is also presented, which is similar to that of the point measurements (figure 4), with a maximum deviation of 8%. This confirms that the luminescence decay dynamics are measured with negligible interference, e.g. from leaking excitation light reflections or fluorescence.

4.4. Precision and accuracy of the approach

To estimate the temperature uncertainty of the approach, measurements on a uniform temperature field, presented in figure 15(a), were considered. For this evaluation, the heating unit was set to maintain a temperature of 37.5 °C behind the plate, as measured by the thermocouple. The temperature image was processed using a binning level of 7 × 7, resulting in 90 × 47 independent measurements over the 48 mm × 87.5 mm usable area of the plate (which corresponds to 22% of the field of view), or a spatial resolution of 0.95 mm. The temperature precision of the approach was estimated as the standard deviation of the temperature data measured over an area of $\sim$19 × 19 mm^2 (9% of the plate

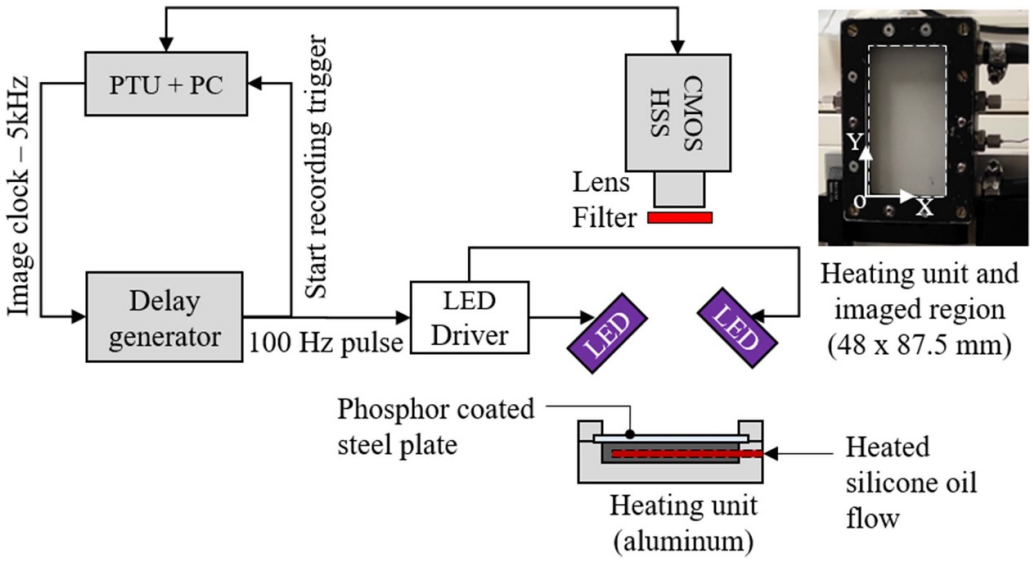

Figure 13. Experimental setup for phase-shift-based phosphor temperature imaging of a temperature-controlled plate.

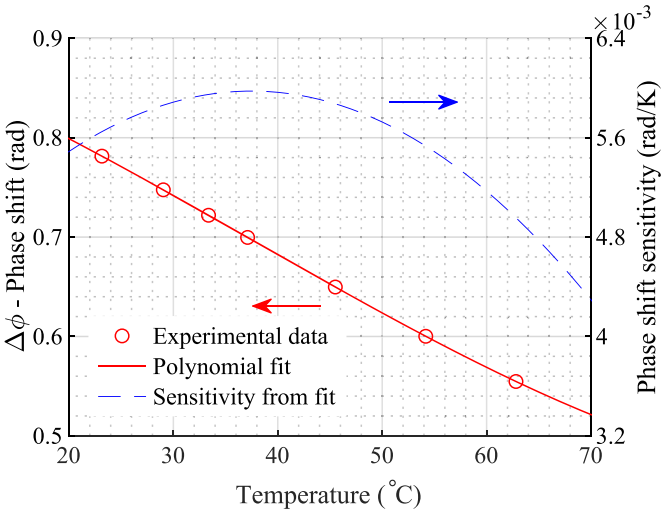

Figure 14. Phase shift-temperature dependence and sensitivity of the imaging system. Experimental data in markers and 3^{rd} order polynomial fit to derive temperature sensitivity in continuous line.

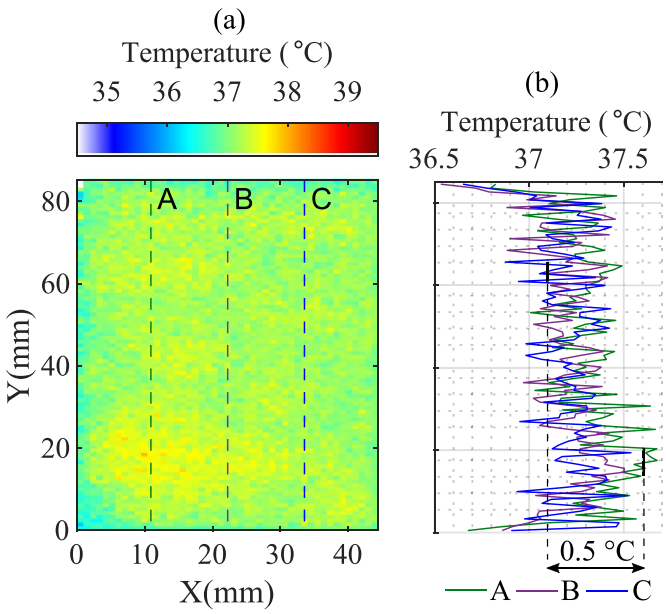

Figure 15. Temperature field measured on the temperature-controlled plate (a) and selected profiles along line A, B and C (b).

area) in the centre of the temperature field where the temperature was assumed uniform. For the reference binning level (7 × 7), the average precision was found to be around 130 mK. Additionally, three vertical cuts ($X_A = 11$ mm, $X_B = 23$ mm and $X_C = 34$ mm) shown in figure 15(b) depict the spatial temperature fluctuations at these locations. By comparing the local maximum temperature observed in the cut A with the local minimum temperature in the cut C, as the worst-case scenario, a maximum systematic temperature error of 0.5 °C can be estimated.

This systematic temperature error can be attributed to different sources, including optical artefacts related to non-uniform coating or illumination, non-uniform pixel sensitivity, as well as physical thermal effects. The latter may include non-uniform heat distribution due to the internal channel geometry or natural convection on the surface, considering the plate was vertical during the experiment.

For this demonstration, the modulation frequency (100 Hz) was chosen to provide best results at the targeted temperature range (30 °C–40 °C). As described in figure 8, for this frequency of 100 Hz, the temperature precision degrades by a factor two at 120 °C compared to 35 °C. Applications that target higher or lower temperature ranges would use a different modulation frequency or a different phosphor, which temperature response is more favourable over the targeted temperature range.

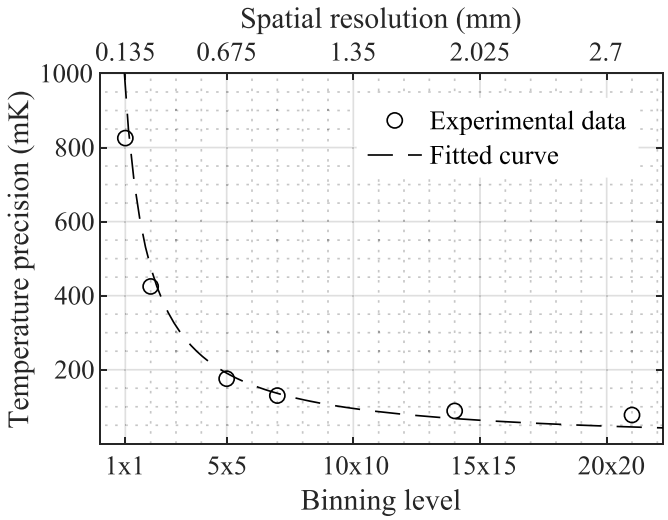

Figure 16. Influence of the image size or spatial resolution (δx) on the spatial temperature precision (σ_T). The experimental data was fitted using a relation where σ_T is inversely proportional to δx.

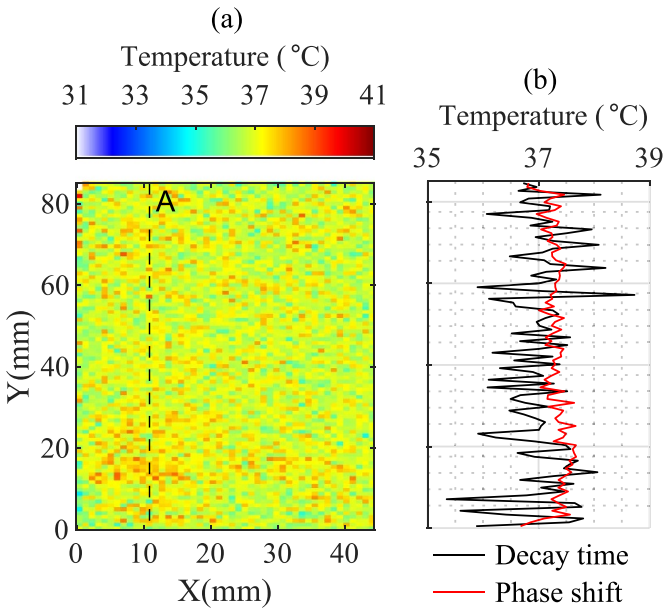

Figure 17. Temperature field on the plate evaluated with decay-time method (a) and comparison of temperature profiles between decay-time and phase-shift method along line A (b).

There is always a compromise between the pixel-to-pixel temperature precision (σ_T) and the spatial resolution (δx). Both should be sufficient to avoid burying the fine temperature dynamics in noise or aliasing effects. In figure 16, the precision is plotted against the spatial resolution. As observed for the temporal resolution in the point measurements (section 3.6), the precision improves as the resolution decreases. Here, the data was fitted with $\sigma_T = K\delta x$ as binning N by N pixels, decreases the spatial resolution by N and represents an ensemble averaging over N^2 pixels, so that the precision decreases with $\sqrt{N^2} = N$.

For this experiment, the highest possible resolution, limited by the imaging system, would be achieved using a binning level of 1×1, corresponding to 630×329 independent pixels with a spatial resolution of 0.135 mm. However, the precision at this level, around 825 mK, would not be sufficient to depict small local temperature variations. On the other hand, low-resolution imaging, such as a 21×21 binning level (30×16 independent pixels), would offer high-temperature precision, but also the possibility of missing local temperature patterns due to aliasing effects. Consequently, a binning level of 7×7 (resulting in a 90×47 pixel image size) was chosen for this demonstration because it offers a good balance between spatial resolution (0.95 mm) and temperature precision (130 mK).

4.5. Comparison with decay-time method

To quantify the improvement that the phase-shift method can offer over the decay-time method in an image configuration, the same recorded datasets used in figure 15 were evaluated using the decay time method. Figure 17(a) shows the resultant temperature image evaluated with the decay time method. It is seen that temperature magnitudes and patterns have the same behaviour as within the phase-shift images, but when examining the vertical cut A, the temperature data based on decay time is significantly noisier than phase-shift-based data, which would worsens the evaluation of temperature gradients.

For the decay-time evaluation, the temperature precision is estimated, from a region in the centre of temperature field, as 0.51 °C, while the phase shift method has a precision of 0.13 °C. This 74% improvement is consistent with the 69% improvement observed on the point-based evaluation with square waveform at 0.2 A in figure 11(b). In the current configuration, unlike the evaluation in section 3.8, the LED driver does not allow an increase in the peak LED drive current.

5. Conclusions

This study has explored theoretically and experimentally the performance of the phase-shift strategy in terms of measurement precision. The phase shift-temperature dependence of YAG:Cr^{3+} phosphor was characterised for different modulation frequencies. The temperature sensitivity was found to be optimised at a phase shift of about $\pi/4$, while the phase shift precision remains constant for values of the phase shift below 0.43π. Therefore, these findings confirm that the optimum modulation frequency is that which is associated with a phase shift of $\pi/4$, i.e. $f = \frac{1}{2\pi\tau}$. We propose an accurate equation to predict the evolution of the temperature precision with modulation frequency and temperature, based on known phosphor-temperature dependence of the decay time. The error of these predictions is only around 10%, which is excellent for experimental design purposes.

The effect of the modulated waveform on the excitation source was studied, and the square waveform was found to be 35% more precise than the sine waveform at low SNR. At

high SNR, the precision is almost independent to the excitation waveform.

The phase-shift method was compared to the most used decay-time method. For the same peak LED current and temporal resolution, the precision of the phase-shift method is three-fold improved with respect to the decay-time method. To obtain a similar level of precision with the decay-time method, the LED peak current needs to be increased by more than 250%, which could be possible for some LED systems owing to the lower duty cycle of the excitation waveform used for the decay-time method.

An implemented temperature imaging configuration, optimised with the findings of the parametric study, yielded a precision of 0.1 °C for an image resolution of 90 by 47 (0.95 mm spatial resolution). Additional spatial evaluation depicted maximum spatial temperature error of 0.5 °C. Overall, the 2D phase-shift based approach demonstrated a 74% improvement in temperature precision compared to the 2D decay time method under identical conditions.

The temporal resolution for the image configuration was 0.25 s, corresponding to 25 cycles. For the phosphor used, the maximum temporal resolution is one cycle or 10 ms. For higher temporal resolution, a faster phosphor should be used such as ScVO4:Bi^{3+} [34], and diode laser modulated at frequencies above 100 kHz as in [18].

This temperature imaging technique, which yields high temperature precision, can be applied in a variety of experimental research fields, for example to study boiling heat transfer, or fine dissipative processes in material deformation analysis, as well as to probe heat generation in electronic or thermochemical devices for thermal management purposes. A subsequent study will apply this thermometry approach to investigate temperature gradients on the surface of a mechanically loaded electrochemical pouch cell during operation. Finally, this study considered rather low temperatures (<200 °C), with respect to what can be achieved with thermographic phosphors (>1000 °C). At higher temperatures, lower luminescence signals, and higher levels of thermal radiation are expected. The phase shift method with a square modulation waveform was found to be well-suited for low-intensity signals. However, it would be interesting to compare the performance of the decay-time and phase-shift methods in cases with significant levels of thermal radiation.

Data availability statement

All data that support the findings of this study are included within the article (and any supplementary files).

Acknowledgments

This work was funded by the Federal Ministry for Economic Affairs and Climate Action (BMWK) through the Zentrales Innovationsprogramm Mittelstand (ZIM) grant – FKZ: KK5264303CM3, and the European Regional Development Fund and the state of Saxony–Anhalt, which are funding the Kompetenzzentrum eMobility (KeM), Grant Number ZS/2018/09/94406. We also thank the technical support of Gunar Boye and Henrik–Christian Graichen. Discussions with Anthony Ojo, Christopher Abram and Fabio Martins are also gratefully acknowledged.

ORCID iDs

Joel López Bonilla https://orcid.org/0000-0002-6288-1996
Frank Beyrau https://orcid.org/0000-0002-8043-7194
Benoit Fond https://orcid.org/0000-0002-8152-4126

References

[1] Meola C and Carlomagno G M 2004 Recent advances in the use of infrared thermography *Meas. Sci. Technol.* **15** 09570233
[2] Meola C, Boccardi S and Carlomagno G M 2015 Measurements of very small temperature variations with LWIR QWIP infrared camera *Infrared Phys. Technol.* **72** 195–203
[3] Sutton G, Korniliou S, Andreu A and Wilson D 2022 Imaging luminescence thermometry to 750 °C for the heat treatment of common engineering alloys and comparison with thermal imaging *Int. J. Thermophys.* **43** 1–26
[4] Liu T and Sullivan J P 2005 *Pressure and Temperature Sensitive Paints* (*Experimental Fluid Mechanics*) 2nd edn (Springer) (https://doi.org/10.1007/978-3-030-68056-5)
[5] Allison S W and Gillies G T 1997 Remote thermometry with thermographic phosphors: instrumentation and applications *Rev. Sci. Instrum.* **68** 2615–50
[6] Aldén M, Omrane A, Richter M and Särner G 2011 Thermographic phosphors for thermometry: a survey of combustion applications *Prog. Energy Combust. Sci.* **37** 422–61
[7] Costantini M, Henne U, Risius S and Klein C 2021 A robust method for reliable transition detection in temperature-sensitive paint data *Aerosp. Sci. Technol.* **113** 106702
[8] Brübach J and Pflitsch C Dreizler A and Atakan B 2013 On surface temperature measurements with thermographic phosphors: a review *Prog. Energy Combust. Sci.* **39** 37–60
[9] Brübach J, Janicka J and Dreizler A 2009 An algorithm for the characterisation of multi-exponential decay curves *Opt. Lasers Eng.* **47** 75–79
[10] Fuhrmann N, Brübach J and Dreizler A 2013 Phosphor thermometry: a comparison of the luminescence lifetime and the intensity ratio approach *Proc. Combust. Inst.* **34** 3611–8
[11] Atakan B, Eckert C and Pflitsch C 2009 Light emitting diode excitation of Cr^{3+} :Al_2O_3 as thermographic phosphor: experiments and measurement strategy *Meas. Sci. Technol.* **20** 075304
[12] Allison S W 2021 On the role of excitation pulse duration on luminescence measurements *Meas. Sci. Technol.* **32** 064007
[13] Feuk H, Nilsson S and Richter M 2022 Laser excitation effects in lifetime-based high-speed phosphor thermometry *J. Lumin.* **250** 119106
[14] McCormack J S H R C 1981 General electric co ltd, Wembley U remote optical measurement of temperature using luminescent materials *Electron. Lett.* **17** 630–1
[15] Vitta P, Pobedinskas P and Žukauskas A 2007 Phosphor thermometry in white light-emitting diodes *IEEE Photonics Technol. Lett.* **19** 399–401
[16] Aizawa H, Sekiguchi M, Katsumata T, Komuro S and Morikawa T 2006 Fabrication of ruby phosphor sheet for

the fluorescence thermometer application *Rev. Sci. Instrum.* **77** 044902
[17] Schreivogel P and Pfitzner M 2015 Optical convective heat transfer measurements using infrared thermography and frequency domain phosphor thermometry *Int. J. Heat Mass Transfer* **82** 299–308
[18] Ojo A O, Fond B, Abram C, Wachem B G M V, Heyes A L and Beyrau F 2017 Thermographic laser doppler velocimetry using the phase-shifted luminescence of bam:Eu^{2+} phosphor particles for thermometry *Opt. Exp.* **25** 11833–43
[19] Torgerson S D, Liu T and Sullivan J P 1996 Use of pressure sensitive paints in low speed flows *Advanced Measurement and Ground Testing Conf. (New Orleans, LA, 17–20 June)* (https://doi.org/10.2514/6.1996-2184)
[20] Yorita D, Henne U, Klein C, Munekata M and Holst G A 2019 Investigation of image-based lifetime psp measurements with sinusoidal excitation light *AIAA Scitech 2019 Forum (California)* pp 1–9
[21] Noda T, Nakakita K, Wakahara M and Kameda M 2018 Detection of small-amplitude periodic surface pressure fluctuation by pressure-sensitive paint measurements using frequency-domain methods *Exp. Fluids* **59** 1–12
[22] Omrane A, Ossler F and Aldén M 2002 Two-dimensional surface temperature measurements of burning materials *Proc. Combust. Inst.* **29** 2653–9
[23] Kissel T, Baum E, Dreizler A and Brübach J 2009 Two-dimensional thermographic phosphor thermometry using a CMOS high speed camera system *Appl. Phys.* B **96** 731–4
[24] Someya S, Uchida M, Tominaga K, Terunuma H, Li Y and Okamoto K 2011 Lifetime-based phosphor thermometry of an optical engine using a high-speed CMOS camera *Int. J. Heat Mass Transfer* **54** 3927–32
[25] Fuhrmann N, Schild M, Bensing D, Kaiser S A, Schulz C, Brübach J and Dreizler A 2012 Two-dimensional cycle-resolved exhaust valve temperature measurements in an optically accessible internal combustion engine using thermographic phosphors *Appl. Phys.* B **106** 945–51
[26] Ojo A O, Escofet-Martin D and Peterson B 2023 High-precision 2D surface phosphor thermometry at kHz-rates during flame-wall interaction in narrow passages *Proc. Combust. Inst.* **39** 1455–63
[27] Venturini F, Bürgi R, Borisov S and Klimant I 2015 Optical temperature sensing using a new thermographic phosphor *Sens. Actuators* A **233** 324–9
[28] Bosselman T, Reule A and Schröder J 1984 Fiber-optic temperature sensor using fluorescence decay time *Proc. Int. Conf. on Optical Fiber Sensors (Stuttgart)* pp 151–4
[29] Cho E and Cho M J 2009 Variance of sample variance with replacement *Int. J. Pure Appl. Math.* **52** 43–47
[30] Zhang Z, Grattan K T V and Palmer A W 1993 Temperature dependences of fluorescence lifetimes in Cr^{3+}-doped insulating crystals *Phys. Rev.* B **48** 7772–8
[31] Liebsch G, Klimant I and Wolfbeis O S 1999 Luminescence lifetime temperature sensing based on sol-gels and poly(acrylonitrile)s dyed with ruthenium metal-ligand complexes *Adv. Mater.* **11** 1296–9
[32] Dragomirov P, Mendieta A, Abram C, Fond B and Beyrau F 2018 Planar measurements of spray-induced wall cooling using phosphor thermometry *Exp. Fluids* **59** 1–13
[33] Mendieta A, Fond B, Dragomirov P and Beyrau F 2019 A delayed gating approach for interference-free ratio-based phosphor thermometry *Meas. Sci. Technol.* **30** 074002
[34] Abram C, Wilson Panjikkaran I, Ogugua S N and Fond B 2020 $ScVO_4$:Bi^{3+} thermographic phosphor particles for fluid temperature imaging with sub-$^{\circ}$C precision *Opt. Lett.* **45** 3893–6